Nucleic Acids Research, 2024, **52**, 10836–10849
https://doi.org/10.1093/nar/gkae749
Advance access publication date: 1 September 2024
Computational Biology

Machine learning unravels inherent structural patterns in *Escherichia coli* Hi-C matrices and predicts chromosome dynamics

Palash Bera* and Jagannath Mondal*

Tata Institute of Fundamental Research Hyderabad, Telangana 500046, India

*To whom correspondence should be addressed. Tel: +91 40 20203091; Email: jmondal@tifrh.res.in
Correspondence may also be addressed to Palash Bera. Email: palashb@tifrh.res.in

Abstract

High dimensional nature of the chromosomal conformation contact map ('Hi-C Map'), even for microscopically small bacterial cell, poses challenges for extracting meaningful information related to its complex organization. Here we first demonstrate that an artificial deep neural network-based machine-learnt (ML) low-dimensional representation of a recently reported Hi-C interaction map of archetypal bacteria *Escherichia coli* can decode crucial underlying structural pattern. The ML-derived representation of Hi-C map can automatically detect a set of spatially distinct domains across *E. coli* genome, sharing reminiscences of six putative macro-domains previously posited via recombination assay. Subsequently, a ML-generated model assimilates the intricate relationship between large array of Hi-C-derived chromosomal contact probabilities and respective diffusive dynamics of each individual chromosomal gene and identifies an optimal number of functionally important chromosomal contact-pairs that are majorly responsible for heterogenous, coordinate-dependent sub-diffusive motions of chromosomal loci. Finally, the ML models, trained on wild-type *E. coli* show-cased its predictive capabilities on mutant bacterial strains, shedding light on the structural and dynamic nuances of ΔMatP30MM and ΔMukBEF22MM chromosomes. Overall our results illuminate the power of ML techniques in unraveling the complex relationship between structure and dynamics of bacterial chromosomal loci, promising meaningful connections between ML-derived insights and biological phenomena.

Graphical abstract

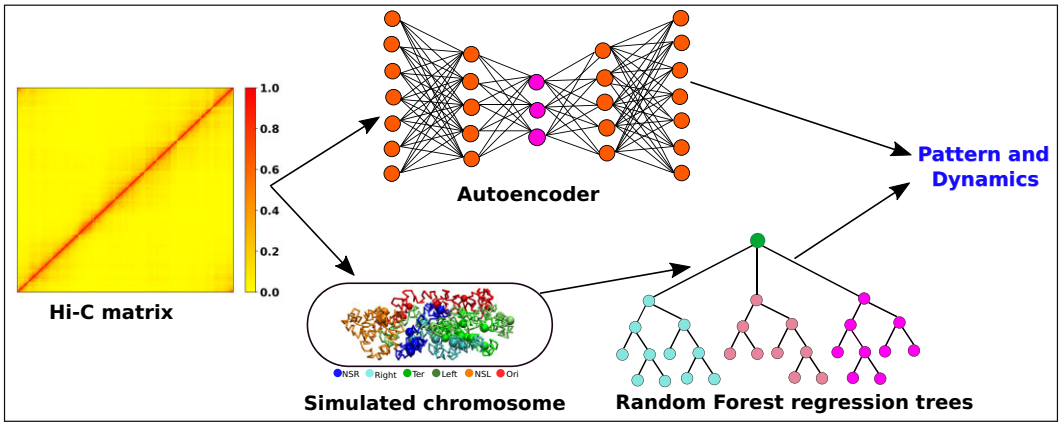

Introduction

The archetypal bacterium *Escherichia coli* possesses a supercoiled circular DNA with a length of 1.6 mm and a size of 4.64 Mega basepair (Mb), confined within a (2–4) μm long spherocylinder (1,2). Over the years, our understanding of the *E. coli* chromosome has evolved significantly. Initially it was thought that chromosome is a just like a complex blob of various macromolecules such as DNA, proteins, RNA, etc. However, subsequent findings (3–6) reveal that, instead of a complex, blob-like architecture, it consists of a well-organized structure with distinct domains known as macro domains(MDs) (7–12). In this regard, various chromosome conformation capture techniques (13–15) provide us with crucial information, unraveling the spatial organization of the genome, especially in understanding higher-order structures. Recent upgrade in high throughput genome sequencing technique (Hi-C) allows to

Received: March 8, 2024. **Editorial Decision:** August 8, 2024. **Accepted:** August 19, 2024
© The Author(s) 2024. Published by Oxford University Press on behalf of Nucleic Acids Research.
This is an Open Access article distributed under the terms of the Creative Commons Attribution-NonCommercial License (https://creativecommons.org/licenses/by-nc/4.0/), which permits non-commercial re-use, distribution, and reproduction in any medium, provided the original work is properly cited. For commercial re-use, please contact reprints@oup.com for reprints and translation rights for reprints. All other permissions can be obtained through our RightsLink service via the Permissions link on the article page on our site—for further information please contact journals.permissions@oup.com.

investigate the three-dimensional conformation of *E. coli* chromosomal DNA (16). This innovative method generates a high-resolution contact map, referred to as the Hi-C matrix which captures the proximity and frequency of contact between various regions of *E. coli* chromosome. Furthermore, the Hi-C matrices for different mutant provide valuable insights into the functions of nucleoid-associated proteins (NAPs) and their roles in maintaining the nucleoid's structure (16). The resulting chromosomal organization significantly influences the dynamic behaviour of chromosomal loci. Previous fluorescence based experimental studies have revealed that these chromosomal loci move subdiffusively (17–20), with their motion strongly influenced by genomic coordinates, showcasing a remarkable level of heterogeneity in their dynamics (19). Integrating this Hi-C-derived contact information into a polymer-based model has enabled development of data-informed integrative studies to furnish a plethora of structural and dynamical details regarding the *E. coli* chromosome (21–24). These theoretical studies achieve a level of experimental accuracy that enhances our comprehension of the intricacies governing the organization and dynamical behavior of the *E. coli* chromosome.

The Hi-C-derived chromosomal contact map represents a multi-dimensional interaction matrix (25,26). Even for a prokaryotic cell such as *E. coli*, with singular circular DNA of 4.6 Mb sequence-length, the Hi-C matrix (16) manifests a dimension as large as (928 × 928) at a 5 Kb resolution. As a result, discerning meaningful information via its visual inspection of extremely large dimensional heterogenous interaction map can be challenging. In recent years, the state of the art machine learning (ML) techniques have emerged as powerful tools for automated extraction of valuable insights from large dimensional data. Notably, most ML-based investigations have centered around eukaryotic chromosomes, benefiting from extensive data sets spanning various replication stages and chromosomes. The inherent complexity of eukaryotic cells, which possess multiple chromosomes, affords opportunities for examining both intra and interchromosomal contacts. These studies are mainly focused on (i) subcompartment annotation of the genome (27,28) by using inter-chromosomal contacts, (ii) enhancing the resolution of Hi-C (29,30) data and (iii) prediction of contact frequency maps using DNA sequence information (31). In contrast, ML-related studies for prokaryotic chromosomes are not as well-developed, primarily due to the challenges posed by the lower resolution and smaller quantity of available data. In light of this, we pose following questions :

- What underlies a ML-derived low-dimensional representation of the Hi-C map of *E. coli* chromosome?
- Can we quantitatively extract a subset of minimal chromosomal contact informations that would sufficiently reconstruct the experimentally observed (19) heterogeneous sub-diffusive motion of chromosomal loci?
- To what extent would the ML-based learning of wild-type chromosomal contact information aid in the prediction of Hi-C map of NAP-devoid mutant?

To address these questions, we first employ an artificial neural network (ANN) based frame-work known as Autoencoder, in a bid to uncover crucial structural insights embedded within this large Hi-C matrix. As would be revealed in first part of Results section, a latent space representation of the Hi-C map successfully identified various MDs with a high degree of accuracy with experimentally derived MDs. In the later part of the manuscript, in a complementary approach, we integrate Hi-C contacts into a polymer-based model, predicting diffusive dynamics of a large number of chromosomal loci using a supervised machine learning technique called Random Forest (RF) regression. As would be unveiled in the manuscript, the proposed regression model successfully recover the coordinate-dependent heterogeneous subdiffusion (19) of chromosomal loci. Moreover, we extract important features from the input data that are crucial in maintaining this dynamical behavior of the loci. By incorporating only these important features related to Hi-C contacts into the polymer model, we successfully reproduce loci dynamics. Finally, we provide our insight on extent of predictive ability of both structure and dynamics of two NAP-devoid mutants of the chromosome (namely ΔMatP30MM and ΔMukBEF22MM) by ML models (Autoencoder and RF) trained on wild-type chromosome.

Results

Unsupervised ML model identifies a meaningful intrinsic structural pattern embedded within the Hi-C matrix of *E. coli* chromosome

Overview of ML architecture

We employed an unsupervised machine learning algorithm known as Autoencoder (32,33) to unveil the essential structural insights embedded within the Hi-C matrix. Autoencoder is a type of unsupervised deep neural network characterized by a dual structure comprising an encoder and a decoder, with a bottleneck in between (Figure 1A). In this architecture, the encoder converts the input data from a high-dimensional space to a lower-dimensional representation known as the latent space. Subsequently, the decoder reconstructs the initial input data from this latent space. This process involves the adjustment of model parameters, primarily weights and biases. Consequently, the compressed representation within the latent space reflects a non-linear transformation of the original input data, encapsulating crucial information or patterns inherent in the input datasets.

In our ML model, the input comprises a single Hi-C probability matrix with dimensions 928 × 928 (4640 kb/5 kb = 928). The Autoencoder architecture is structured with a total of nine sequential layers featuring neuron counts of 928, 500, 200, 100, L_d, 100, 200, 500 and 928, respectively, where L_d denotes the dimension of the latent space. After setting up the Autoencoder architecture, we need to choose L_d judiciously. To determine this dimension, we computed the Fraction of Variance Explained (FVE) through reconstruction, which is defined as

$$\mathrm{FVE} = 1 - \frac{\sum_{i=1}^{N} \|\mathbf{I}(i) - \mathbf{O}(i)\|^2}{\sum_{i=1}^{N} |\mathbf{I}(i) - \bar{\mathbf{I}}\|^2} \quad (1)$$

Here, $\mathbf{I}(i)$, $\mathbf{O}(i)$ and $\bar{\mathbf{I}}$ represent the input, output, and mean input, respectively, and $N = 928$ corresponds to the number of rows in the Hi-C matrix. Figure 1(B) represents the variation of the FVE as a function of latent dimension. We opted for a latent dimension of $L_d = 3$, as it helps to achieve an FVE of at least 0.85, meaning that the Autoencoder's reconstruction accounts for a minimum of 85% of the variance in the input Hi-C data. This choice of latent space dimension not only

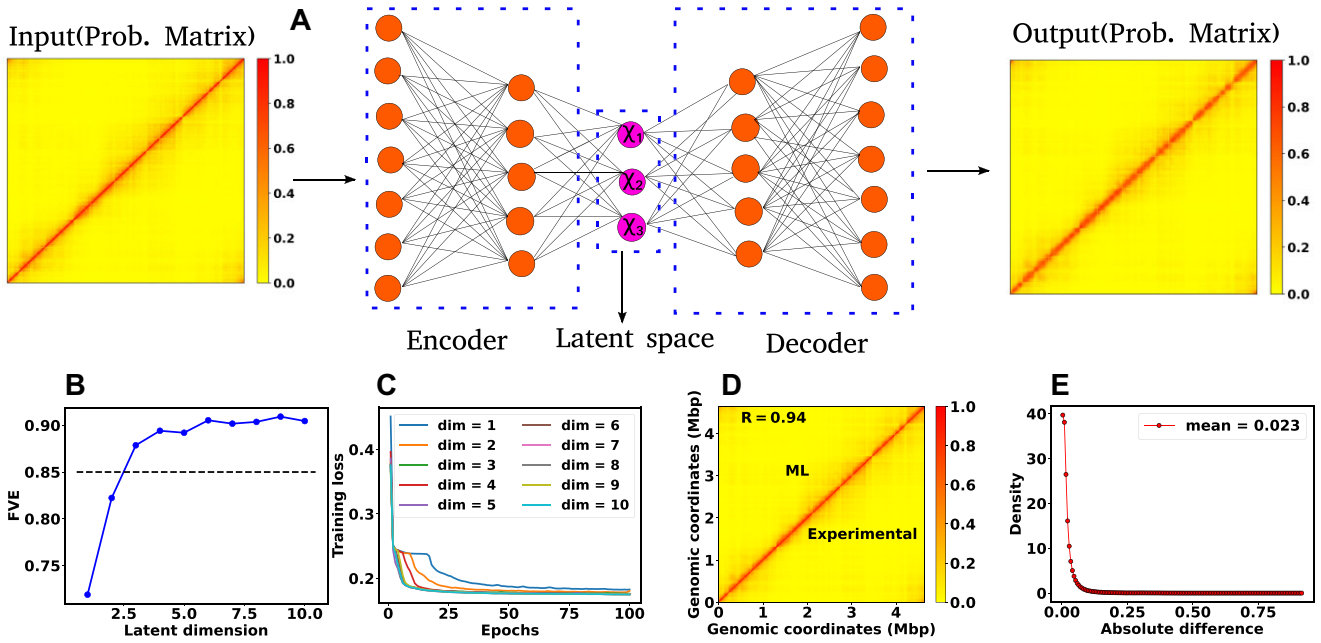

Figure 1. Architecture of the Autoencoder and training robustness. (**A**) Schematic of the Autoencoder, an unsupervised machine learning algorithm. It consists of an encoder and a decoder and in between there is a bottleneck. The encoder transforms high-dimensional input data to a lower-dimensional latent space, while the decoder reconstructs the initial input data from the latent space. This process involves adjusting model parameters, primarily weights, and biases. Each dimension in the latent space corresponds to a latent variable. Here, χ_1, χ_2 and χ_3 represent three latent variables. (**B**) The variation of FVE with respect to the latent dimension (L_d). A $L_d = 3$ was chosen, ensuring an FVE of at least 0.85, signifying that the Autoencoder's reconstruction captures a minimum of 85% of the variance in the input data. (**C**) Training loss as a function of epochs for different latent space dimensions (L_d). Notably, the training loss achieves saturation for all $L_d > 1$ beyond 25 epochs. (**D**) Genome-wide contact probability map between the experimental and ML-derived Hi-C matrix. (**E**) Histogram of the absolute difference between experimental and ML-derived contact probability matrices. The Pearson correlation coefficient(PCC) is 0.94, and the absolute difference in mean values is 0.023, indicating a substantial agreement in chromosomal interactions.

ensures effective data representation but also affords flexibility in visualizing the compressed data.

To assess the training robustness across various latent space dimensions (L_d) concerning the number of epochs, we have plotted the training loss as a function of epochs for different L_d (Figure 1(C)). The figure clearly illustrates that beyond epochs = 25, the training loss reaches a point of saturation for all $L_d > 1$. This observation implies that selecting a number of epochs greater than 25 is a prudent choice. In our model, we opted for 100 epochs and in the Method section, additional specifics regarding the training of the Autoencoder are discussed. In a similar vein, we conducted a comparison between the input (experimental) and output (reconstructed) matrices. Figures 1(D) and (E) compare the genome-wide contact probability map between the experimental and ML (reconstructed by the Autoencoder with $L_d = 3$) contact probability matrix, along with a histogram showing the difference between the two matrices. Our findings reveal a Pearson correlation coefficient (PCC) of 0.94 between the experimental and ML contact probability matrices. Additionally, the absolute difference in the mean values is 0.023, indicating a substantively strong agreement between experimental and ML-derived chromosomal interactions.

The pattern emergent from latent space of the ML-model recovers key Macro-domains across *E. coli* genome

We aim to understand the biological significance of the lower-dimensional representation ($L_d = 3$) of the input data. To achieve this, we generated a scatter plot of the latent space data and conducted clustering using the K-means algorithm (34,35). Our hypothesis is that each cluster signifies specific domains within the bacterial chromosome, inherently encoded in the Hi-C matrix. Biologically, these large-scale structurally distinct domains are referred to as macrodomains(MDs) (7–12). It is noteworthy that the actual molecular mechanisms governing macrodomain organization remain incompletely understood, and the precise boundaries of these MDs have been found to vary across different reports (7–11). For example, in 2000, Niki *et al.* (7) identified mainly four macrodomains: Ori, Right, Ter and Left. Later, other experimental studies by Valens *et al.* (8) and Espéli *et al.* (10) identified two more macrodomains, NSR and NSL. The variations in macrodomain boundaries observed across different studies are primarily attributed due to the applied method itself (12). In our study, we have utilized the MDs boundary as reported by Espéli *et al.* (10) which is more recent.

In Figure 2(A), a scatter plot illustrates the three dimensional ($L_d = 3$, χ_1, χ_2 and χ_3) representation of the latent space, with distinct color-coded clusters representing various MDs of the chromosome. From experimental study (10), we possess a priori knowledge regarding the base pairs of each macrodomain. Additionally, through clustering, we have obtained base pair information for each macrodomain. Subsequently, we conducted a detailed comparison between experimentally denoted and (ML)-derived MDs by schematically drawing the DNA as a circle (Figure 2B). The inner and outer circles, featuring various color-coded regions, represent the experimentally denoted and ML-derived macrodomains, respectively, with base pair information annotated in kilo bases (kb).

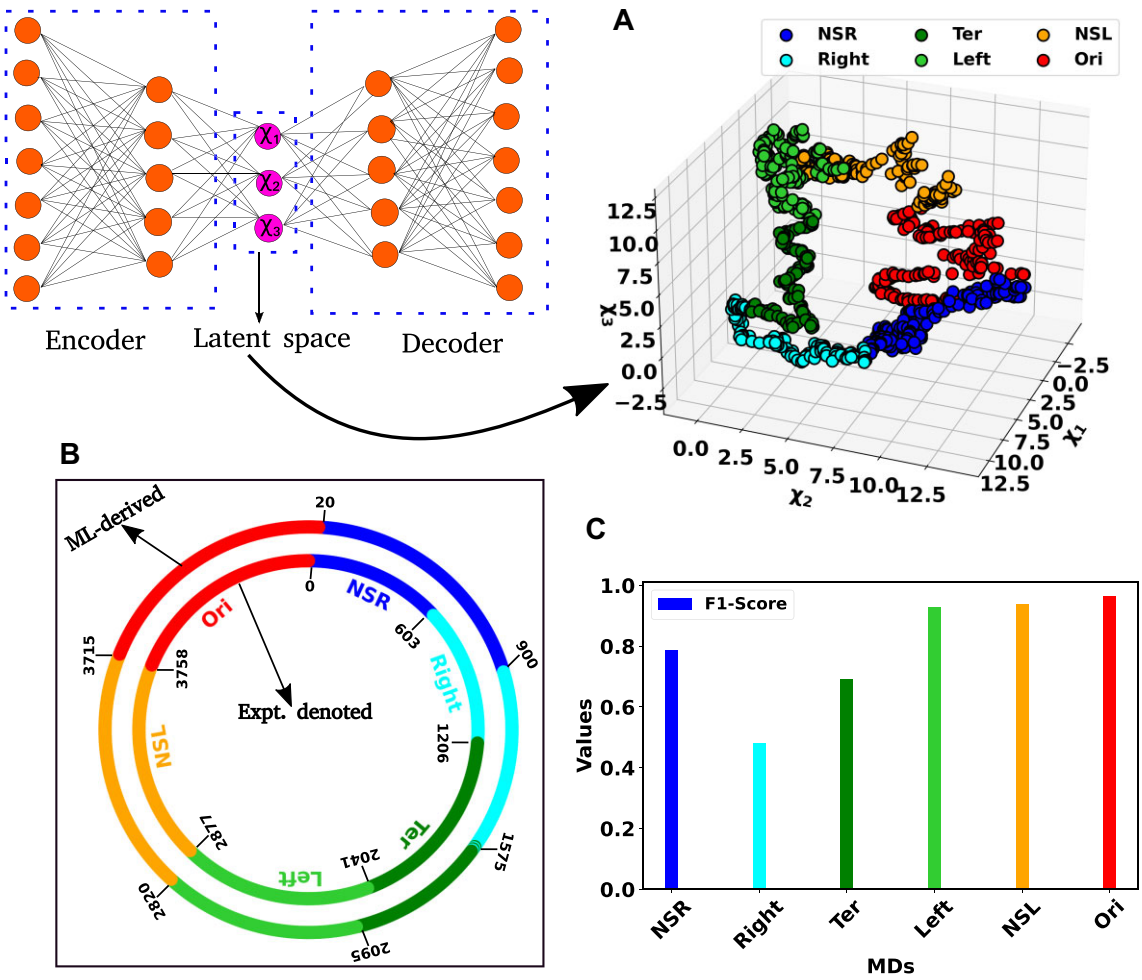

Figure 2. Representation of the latent space and classification of different macrodomains. (**A**) Three dimensional scatter plot of the latent space variable χ_1, χ_2 and χ_3. The data has been clustered using K-means clustering. The various color-coded clusters are representing distinct macrodomains (MDs) within the bacterial chromosome. (**B**) The comparison between experimentally denoted and machine learning (ML)-derived MDs. The inner and outer circles, each encoded by various color-coded regions, delineate the experimentally denoted and ML-derived macrodomains, respectively, with base pair information annotated in kilo bases (kb). (**C**) The bar plot of the F1-score for different MDs. The higher values of the F1-Score indicated the better classification.

A visual inspection indicates substantial agreement between MDs, barring discrepancies in the NSR, Right, and Ter MDs. Quantitative comparison between actual (experimentally denoted) and predicted (ML-derived) MDs is facilitated by the confusion matrix (see SI for details). Metrics such as Accuracy, Precision, Recall, and F1-Score can be computed from the confusion matrix as follows.

$$\text{Accuracy} = \frac{TP + TN}{TP + TN + FP + FN}$$

$$\text{Precision} = \frac{TP}{TP + FP}$$

$$\text{Recall} = \frac{TP}{TP + FN}$$

$$\text{F1-Score} = 2 \times \frac{\text{Precision} \times \text{Recall}}{\text{Precision} + \text{Recall}}$$

where *TP*, *TN*, *FP* and *FN* stand for 'True Positive', 'True Negative', 'False Positive' and 'False Negative', respectively. Figure 2(C) shows a bar plot of the F1-score for each MD. F1-scores exceeding 0.92 for the Left, NSL MDs suggest a strong match between actual and predicted classes. Conversely, lower F1-Scores for the other three MDs indicate a moderate alignment, consistent with observations in Figure 2(B). Nevertheless, the overall accuracy for all classes stands at 0.82, indicative of a robust correlation between experimentally denoted and ML-predicted MDs. In summary, our unsupervised ML model (Autoencoder) offers a potent automated approach for MDs identification, demonstrating a high degree of accuracy with experimentally derived MDs.

ML-based identification of genomic contacts crucial for *E. coli* heterogeneous dynamics

In the preceding section, we delved into the intrinsic structural properties of *E. coli* chromosome embedded within the Hi-C matrix, which led to an automated discovery of segmented macrodomains in a ML-derived low-dimensional subspace. In this section, we now pose the question: Can we identify the crucial subset of chromosomal contacts in Hi-C map, that hold key to the heterogenous, cooordinate-dependent diffusivities (19,22) of chromosomal loci? Towards this end, we employed a ML-based protocol namely Random Forest Regression to extract dynamical information by leveraging the structural properties of the chromosome, such as the pairwise

distance between chromosomal beads. This supervised, trees-based algorithm, initially proposed by Breiman *et al.* (36,37), is a potent tool widely used for both classification and regression tasks. Random Forest Regression operates by randomly selecting input data from training datasets and creating an ensemble of trees (forests) based on these features and labels of the input data. These ensembles of trees are called 'decision trees'. The final results are derived by averaging (for regression) or voting (for classification) from the outputs of these decision trees. Notably, the Random Forest possesses a distinctive ability to pinpoint the most crucial features within the training datasets.

Data preparation and supervised ML architecture

We implemented a bead-in-a-spring polymer model to simulate the bacterial chromosome and generated a set of 200 distinct initial DNA configurations. In brief, the resolution of each bead is 5×10^3 bp (5 kb), similar to the Hi-C matrix resolution (16). Each bead has a diameter denoted by σ, and the chromosome is confined within a spherocylindrical boundary that mimics the cell wall. The bonded interactions between adjacent beads have been modeled by harmonic springs, while the non-bonded interactions are represented by the repulsive component of the Lennard-Jones potential $V_{nb}(r) = 4\epsilon(\sigma/r)^{12}$, where ϵ is the potential depth, and r is the distance between two beads. The Hi-C interactions are also modeled as effective springs with a spring constant and bond lengths dependent on the strength of the contact probabilities. Following energy minimization of the initial configurations, Brownian Dynamics simulations are conducted for each configuration at a temperature of $k_BT = 1.0$ and friction $\gamma = 1.0$. The length and time scales are represented in the unit of σ (the diameter of each bead) and $\tau_{BD} = \frac{\sigma^2\gamma}{k_BT}$ (Brownian time), respectively throughout the manuscript. The simulations are run for a time duration of $10^3\tau_{BD}$ with a time step $\delta t = 1 \times 10^{-4}\tau_{BD}$, ensuring proper equilibration of each configuration. After equilibration, the pairwise distances are computed using the last snapshot of each run (totaling 200), serving as features for our machine-learning model. The dynamics of each DNA bead are quantified by calculating the mean squared displacement (MSD). For this measurement, we simulate each equilibrium configuration 40 times through Brownian dynamics simulations, drawing distinct velocities from the Maxwell–Boltzmann distribution at a desired temperature of $k_BT = 1.0$. These trajectories, with varying initial velocities, are called isoconfigurational ensembles (38,39). Each ensemble simulation was carried out for a duration of $100\tau_{BD}$. We computed the MSD of each particle i and averaged over the different runs (isoconfigurational ensembles) i.e.

$$\mathrm{MSD}_i(t) = \left\langle |\vec{r}_i(t) - \vec{r}_i(0)|^2 \right\rangle_{\mathrm{runs}} \quad (2)$$

where $\vec{r}_i$ represents the position of ith particle and angular bracket signifies the average over isoconfigurational ensembles. So from the equilibrium configuration, we have calculated the pair-wise distance of the chromosomal beads and the MSDs of individual beads from the isoconfigurational ensembles. These two quantities serve as features and labels, respectively, for our machine-learning algorithm, Random Forest. By using this technique we can predict the dynamics of bacterial chromosomal loci and extract the important chromosomal contact features which are necessary to maintain the dynamics. The entire process of data preparation and the machine learning architecture are schematically depicted in Figure 3A and B, respectively.

Comparison between the actual and ML-predicted MSDs of different loci and their exponents

Upon training the Random Forest regression model, we proceeded to predict the dynamics of individual chromosome loci. The selection of specific loci was based on a prior experimental study conducted by Javer *et al.* (19), which suggested that chromosomal loci belonging to the Ter region exhibit slower motion, while those in the Ori region demonstrate faster motion. To assess the accuracy of ML predictions, we computed the PCC, denoted by ρ, between the predicted and actual MSD values. Figure 4A shows the variation of ρ as a function of time. Remarkably, the correlation ρ exhibits higher values (>0.8) for shorter time intervals. However, the correlation shows a slight decrease for longer duration. Now we will delve into the dynamic properties of distinct loci within the DNA. Each macro domain is comprised of various loci identified by Espeli *et al.* (10) based on their genomic coordinates. Figure 4B represents the comparison between the actual and predicted MSD as a function of time for two distinct loci, Ori2 and Ter3. This figure distinctly reveals a close alignment between the actual MSDs (solid line) and the predicted MSDs (dotted line).

Now, we aim to characterize the type of diffusion for individual loci. In Figure 4C, we present an equilibrated snapshot of the bacterial chromosome, with each color-coded chunk depicting a distinct macrodomain(MD). Each MD is comprised of various loci represented as spherical beads. We fitted the MSD values (both actual and predicted) of each individual loci with a power law:

$$\mathrm{MSD}_i(t) = 6Dt^{\alpha} \quad (3)$$

where t, D and α are the time, diffusion constant, and exponent, respectively. Depending on the exponent α, one can categorize the type of diffusion; for example, $\alpha = 1$ corresponds to normal diffusion, $\alpha < 1$ signifies subdiffusion, and $\alpha > 1$, indicates superdiffusion. Figures 4D and E depicts the comparison of MSD exponents between actual and ML-predicted values for two different time intervals, namely $(0.1-10)\tau_{BD}$ (short time) and $(10-100)\tau_{BD}$ (long time), respectively. From these figures, it is evident that for the short time, the actual MSD exponents for all loci closely match the predicted exponents. However, for the long time, there is a slight deviation in exponents between the actual and predicted values. As the PCC between the actual and predicted MSD values deviates for longer times (as seen in Figure 4A), this discrepancy is also reflected in the exponent values. However, for both timescales, the observed and predicted dynamics exhibit subdiffusion, showcasing significant variability along the genomic coordinates, thereby indicating a heterogeneous nature of the dynamics. We found the ML-model to be robust against multiple hyperparameter (see Figure S1a, b) and related supplemental results SR1).

To get a better insight into these deviations, we have calculated the Pearson correlation coefficient (PCC) between the actual and predicted MSD values over a long time range $(100-500)\tau_{BD}$. Supplementary Figure S2A shows the PCC as a function of time, with the relevant time window highlighted by vertical lines. The figure indicates that PCC values decrease over time. As we use structure-based features (pairwise distance) to predict dynamics, the model starts to forget

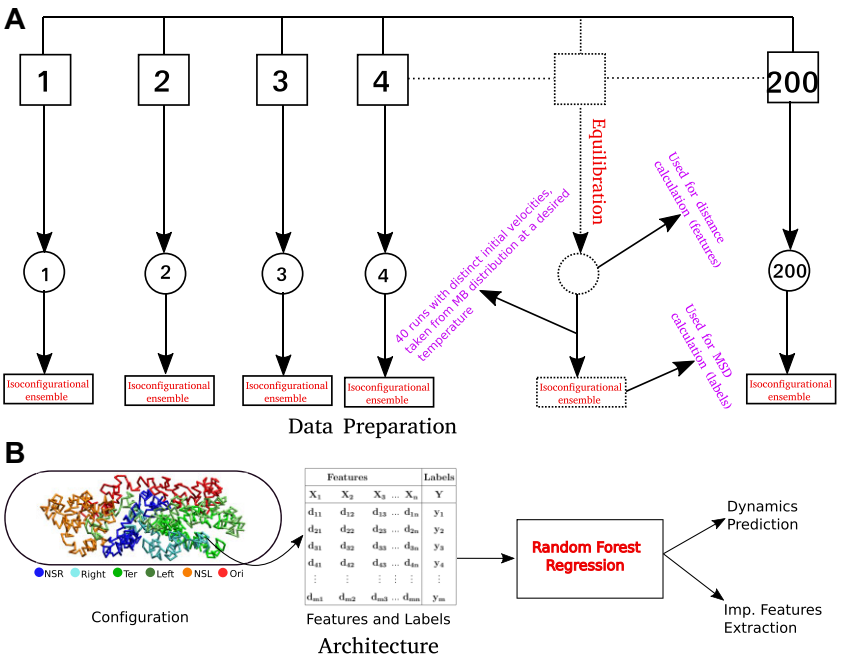

Figure 3. Schematic representation of the Data preparation and the architecture of Random Forest (RF) regression model. (**A**) Data Preparation: At the very beginning we generated a set of 200 distinct initial configuration of DNA using bead-in-a-spring polymer model. We ran the Brownian dynamics simulation for each configuration for a time span of $10^3\tau_{BD}$,to ensure proper equilibration. Following equilibration, pairwise distances were computed using the last snapshot of each run (totaling 200), serving as features for our machine-learning model. For the MSD measurement, we simulate each equilibrium configuration 40 times through Brownian dynamics simulations, drawing distinct velocities from the Maxwell–Boltzmann distribution at a desired temperature of $k_BT = 1.0$. These ensemble (40 trajectory each) are called iso-configurational ensembles. (**B**) Architecture: We utilized the pair wise distance between beads and MSDs of each bead. These two quantities serves as features and labels respectively, in our ML model(RF). After training of the Random Forest (RF) with this datasets, we predicted the dynamics of individual beads. For training and testing, 75% and 25% of the total datasets, were used. Additionally, from the trained model, we extracted important features contributing to the maintenance of dynamical properties.

initial structural information over longer timescales, potentially causing a decrease in PCC values. This effect is also evident in the MSD exponent values (Supplementary Figure S2B). At longer times, the MSD exponents exhibit heterogeneous subdiffusion, but there is a deviation between the predicted and actual MSD exponents. However, these deviations are not substantial. Converting the reduced time unit to actual values shows that $500\tau_{BD} = 100$ min ($1\ \tau_{BD} \approx 12$ s), which is longer than the cell division time of *E. coli* (∼75 min) (19). Therefore, one should consider the replication and segregation in our model. In our study, we used a time of $100\tau_{BD} = 20$ min, which is much shorter than the cell division time in minimal medium. This is also consistent with our previous study (22).

Identifying important chromosomal contact features crucial for loci dynamics

In general, the RF enlightens us about the quantitative extent of significance of each feature by evaluating its impact on impurity. In classification tasks, impurity is assessed through Gini impurity or information gain, while in regression, it involves variance reduction (36,37). During the training, within the decision trees, the greater the reduction in impurity caused by a feature, the more pivotal that feature becomes. In our RF regression model, we have a total of 928 inter-gene distance-based features. Each feature represents the distance between one particular DNA beads with all other beads. To explore the time-dependent importance of these features, we computed cumulative sums of feature importance. Figure 5A–D depicts the cumulative sums of feature importance as a function of the total number of features for different time points: $0.1\tau_{BD}$, $1.0\tau_{BD}$, $10.0\tau_{BD}$, and $100.0\tau_{BD}$, respectively. In each plot, the vertical black dotted line highlights the number of features that contribute to 85% of the total feature importance score. We named the particular number of features as *top features*. A closer examination of the black dotted lines reveals that the number of *top features* is dynamic i.e. varying with time.

To get deeper insights into the feature importance, we have selected the *top features* at a particular time ($t_{\max}^{\mathrm{PCC}}$) when the PCC between the actual and predicted MSDs becomes maximum. In this context, we pinpointed a total of 466 *top features* representing the 85% of the total feature important score. Within the set of 466 *top features*, we computed the percentage-wise contributions from each macrodomain. Figure 5E represents the bar plot of the % of *top features* with respect to different macrodomains. Quite interestingly the percentage-wise contribution of *top features* is not uniform with respect to the various macrodomains. Specifically, Ori MD exhibits the most substantial contribution, whereas Right MD demonstrates a comparatively smaller contribution. In the same spirit, we also identified the *top features* that remain common across different times, totaling 207 in number. Subsequently, we have also plotted the percentage-wise contributions of common *top features* from each macrodomain (Supplementary Figure S3). The plot shows a very similar trend as Figure 5E.

To understand this nonuniform contributions of MDs in feature importance, we have plotted the distribution of the MSD values for different MDs at the specific time point ($t_{\max}^{\mathrm{PCC}}$).

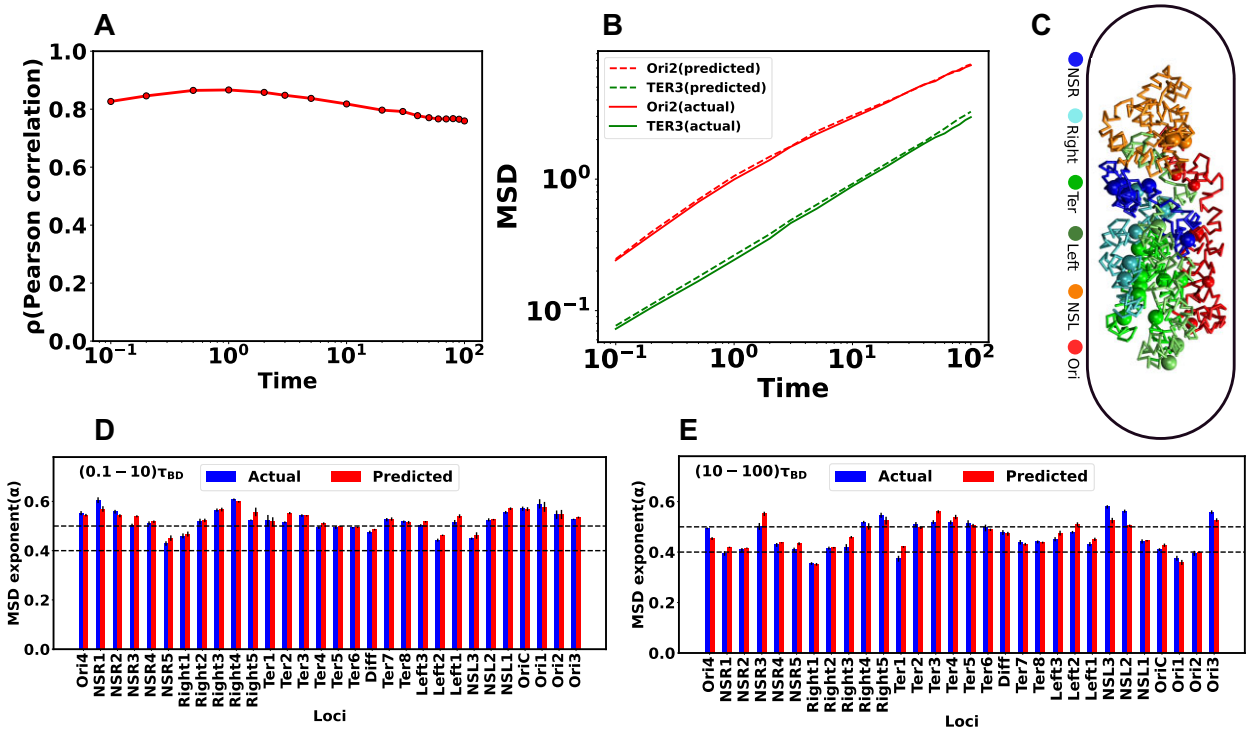

Figure 4. Comparison between the actual and predicted MSD values and their exponents. (**A**) Pearson Correlation Coefficient (PCC) between actual and predicted MSDs as a function of time. During shorter time intervals, PCC demonstrates higher values (>0.8). Conversely, there is a marginal decrease in the PCC for longer time intervals. (**B**) Comparison of actual and predicted MSDs as a function of time for two particular loci Ori2 and Ter3. The dotted line represents the predicted MSDs, while the solid line depicts the actual MSDs. These plots illustrate a notable concordance between the observed and predicted MSDs. (**C**) Equilibrated snapshots of the simulated chromosome. The macrodomains are highlighted by distinct color-coded chunks, and the loci associated with each macrodomain are depicted through a spherical bead representation. Comparing the MSD exponents between observed and predicted values is illustrated for two distinct time intervals: (**D**) $(0.1-10)\tau_{BD}$ (short time) and (**E**) $(10-100)\tau_{BD}$ (long time). Notably, all loci exhibit heterogeneous subdiffusive motion, irrespective of the time intervals. During the short time, the actual MSD exponents for all loci closely align with the predicted exponents. However, for the long time, a slight deviation in exponents between the actual and predicted values becomes apparent. In all the plots, both the MSD and time are expressed in terms of σ^2 and τ_{BD} respectively.

Figure 5F shows the distribution of the MSD values for all the MDs and the standard deviation of each distribution is reported in the legend of the plot. Notably, the plot reveals a significantly broader distribution of MSD values for Ori MD in comparison to Right MD. In the context of our machine learning model, where MSD values serve as labels for supervised learning, these findings imply that the RF regression model requires a greater number of features to construct accurate decision trees when faced with a broad distribution of training data, and conversely, fewer features are needed in the case of a narrower distribution

Can chromosome dynamics be reconstructed using only ML-derived important features?

For a more comprehensive grasp of functional implication of the ML-derived *top features*, we decided to consider only these particular distance-based chromosomal contact features from Hi-C map and incorporate them in our particle-based DNA model. Precisely, originally totaling 17 302 Hi-C contacts, we have now reduced it to 12 233, resulting in a notable reduction of approximately 29%.

By incorporating these subset of Hi-C contacts, we conducted a new set of simulations and compared the outcomes with our initial modelling results. We named the previous set as 'actual' and the current one as 'UTF' (using top features). Figure 6A showcases a heat map of Hi-C contact probability, where the upper and lower triangular matrices represent simulated (UTF) and experimental contact probabilities, respectively. The high PCC of 0.90 between these matrices signifies robust agreement. In terms of dynamics, we have also calculated the MSD exponent of each loci. Figure 6B and C presents bar plots of the MSD exponent for all loci at two timescales: $(0.1-10)\tau_{BD}$ and $(10-100)\tau_{BD}$, respectively. At a shorter time scale, the MSD exponent between the actual and UTF aligns well. However, deviations emerge at longer timescales. These deviations are believed to originate from the dynamic nature of *top features*. From Figure 5A–D, it is clear that the number of top features varies largely over time. But in our new set of simulations (UTF), we have only incorporated the *top features* related Hi-C contacts, at a particular time when the PCC between the actual and predicted MSDs becomes maximum. This modelling approach may overlook crucial features relevant for later times, impacting the accuracy of the exponent. Additionally, Figure 4A shows that the PCC between the actual and predicted MSDs is lower at a longer time. These effects will always provide the deviation of the exponent at a larger time scale irrespective of the time-dependent features engineering.

Nevertheless, the deviations of the exponent are not so huge. Based on this observation, we can assert that RF regression is a powerful technique for predicting dynamics and engaging in feature engineering. The concept of important

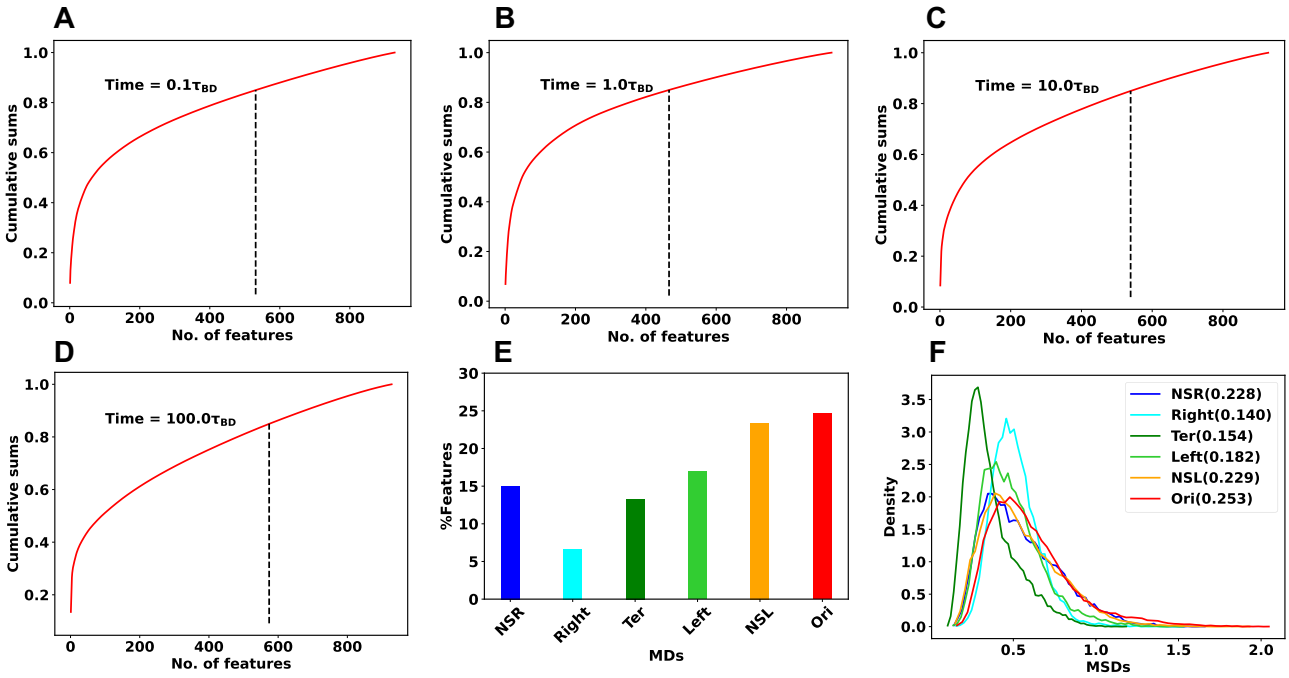

Figure 5. Important features specific to each macrodomain. Cumulative sums of feature importance as a function of the total number of features for different time points (**A**) $0.1\tau_{BD}$, (**B**) $1.0\tau_{BD}$, (**C**) $10.0\tau_{BD}$ and (**D**) $100.0\tau_{BD}$ respectively. Each plot includes a vertical black dotted line indicating the number of features responsible for 85% of the overall feature importance score (referred to as *top features*). The number of *top features* is varying with time. (**E**) The bar plot of the percentage-wise contributions of *top features* with respect to different macrodomains. Notably, Ori MD exhibits a predominant share of *top features*, while Right MD showcases a comparatively smaller proportion of these *top features*. (**F**) Distribution of the MSD values for all the MDs at the specific time point. The standard deviation of each distribution is reported in the legend of the plot. Notably, Ori MD shows a wider distribution compared to Right MD.

features allows us to extract the effective Hi-C contacts that can qualitatively provide the structure and dynamics.

Probing prediction ability of ML-model on NAP-devoid Mutant

To what extent can ML recreate Hi-C matrix of Mutant chromosome?

E. coli intricately maintains a chromosome architecture characterized by distinct macrodomains. Several proteins are responsible for this structural management. These proteins, known as nucleoid-associated proteins (NAPs), contribute to the orchestration of chromosomal organization (40,41). Within this category, certain NAPs exhibit localized binding to chromosomes, while others engage in nonspecific binding. These multifaceted NAPs play discernible roles in shaping the overall organization of the chromosome. Among the NAPs, MatP stands out as a key player responsible for isolating the Ter MD from the rest of the chromosome. Specifically, MatP exhibits specific binding to 23 sites within the Ter MD, known as matS sites (11,42). Notably, in the absence of MatP, there is an enrichment in long-range contacts within the Ter MD and its adjacent domains (16). Another essential protein in the realm of chromosomal structure maintenance is MukBEF, which actively facilitates long-range contacts outside the Ter MD (43). Interestingly, when MukBEF is absent, a reduction in long-range contacts is observed across all MDs except for the Ter MD (16).

We decided to investigate the extent of feasibility of recreating Hi-C matrices for two distinct mutants, namely ΔMatP30MM and ΔMukBEF22MM, using the ML model(Autoencoder) that we had trained on wildtype (WT30MM) Hi-C map. This approach would allow us to assess the extent of intrinsic information within the WT matrix that contributes to the accuracy of reconstructing the chromosome contact map of mutants. Importantly, we do not intend to retrain the model with mutant data. Rather, the ML model (Autoencoder) aims to utilize the pre-optimized weight and bias values derived from the WT Hi-C data to generate the mutant Hi-C matrices.

In Figure 7A and Supplementary Figure S4A, we compare the contact probability maps of the experimental and recreated Hi-C matrices for ΔMatP30MM and a histogram illustrating the matrix differences respectively. The substantial agreement between these matrices is emphasized by a PCC value of 0.92 and an absolute difference in mean values of 0.027. For a more detailed examination of the Hi-C matrices, we computed PCC within distinct macrodomains (MDs) (Figure 7B). The correlation is notably high between individual MDs and their adjacent MDs, contrasting with the lower correlation observed for MDs that are farther apart. While the experimental and recreated matrices may seem similar at first glance, a closer examination through a heat map of their differences reveals specific dissimilarities (Figure 7C). Notably, there is a butterfly-shaped region in the Ter and its adjacent domains, highlighted within the magenta box. These findings imply that the recreated Hi-C fails to accurately capture the interactions within the Ter and its flanking domains. Similarly, in Figure 7D, Supplementary Figure S4B, and Figure 7E, we depict the contact probability map, distribution of the difference in the contact matrix, and MDs-wise PCC between the experimental and recreated Hi-C matrices of ΔMukBEF22MM. The overall PCC (0.92), mean difference values (0.03), and individual PCC of each MD indicate a robust agreement between

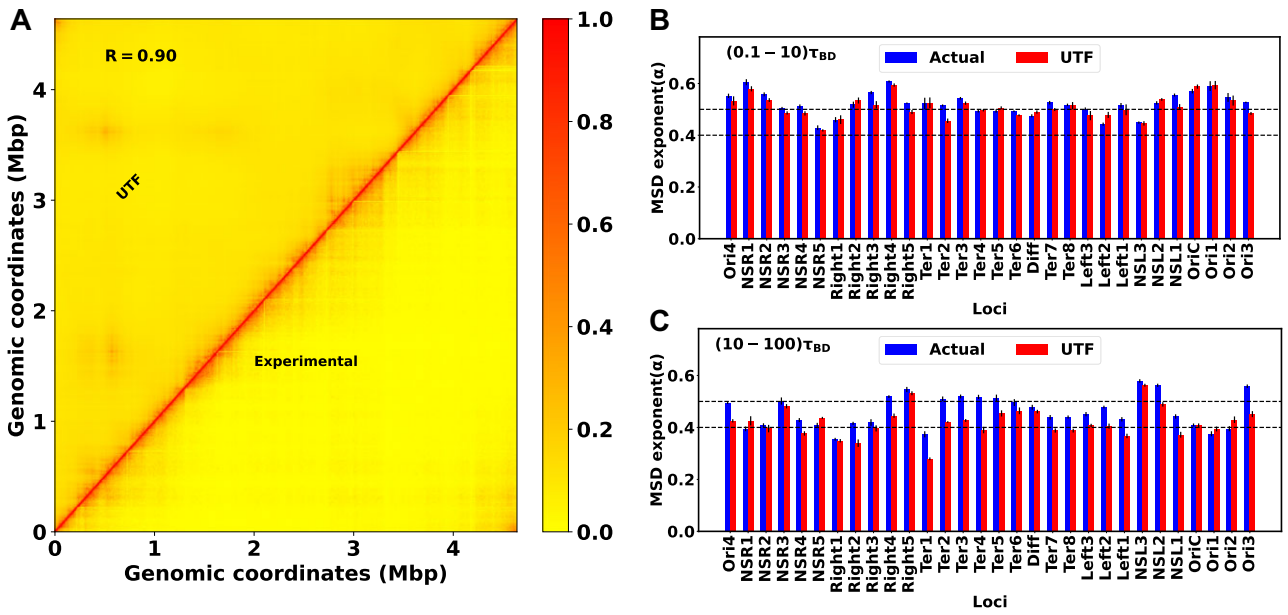

Figure 6. Reproduce the structure and dynamics by using important features. (**A**) The heat map between the experimental and simulated (UTF) contact probability matrix for WT30MM. A PCC value of 0.90 between these matrices indicates strong agreement. The bar plot of the MSD exponent for different loci at two timescales: (**B**) $(0.1-10)\tau_{BD}$ and (**C**) $(10-100)\tau_{BD}$, respectively. At a shorter time scale, the MSD exponent between the actual and UTF matches quite well. However, at a larger time scale, they start to deviate.

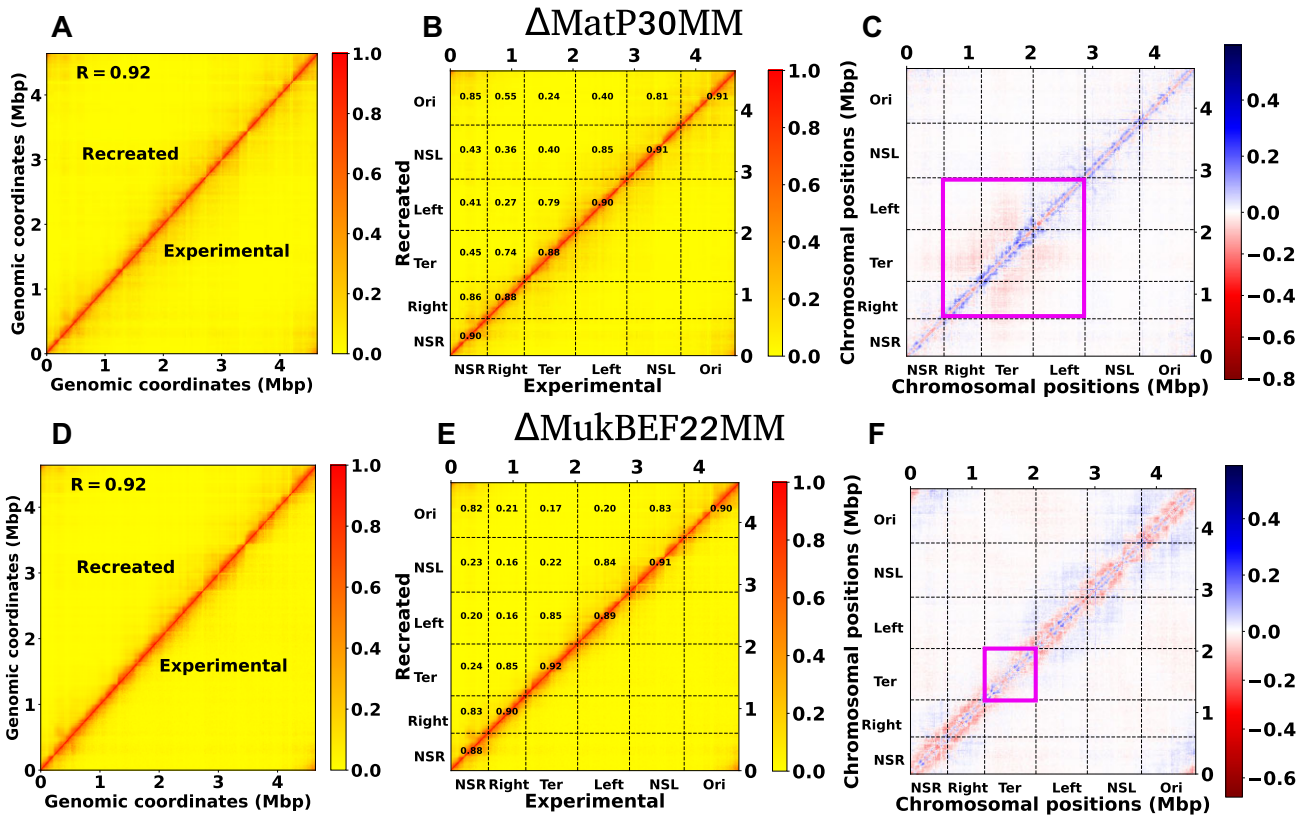

Figure 7. Recreation of the Hi-C matrix for different mutant by using machine learning trained model on wild type Hi-C matrix. (**A**) Heat map between the experimental and ML recreated contact probability matrix for ΔMatP30MM. A Pearson correlation coefficient(PCC) value of 0.92 indicates a reasonably strong agreement between them. (**B**) Within the heat map of the contact probability matrix, individual PCC values for each MD are presented. The PCC are notably high between individual MDs and their adjacent MDs. (**C**) The heat map of the difference matrix (experimental and ML recreated) reveals a butterfly-shaped region inside the Ter and its flanking domains, denoted by the magenta box. This observation suggests that the ML-recreated matrix fails to accurately capture the interactions within the Ter and its nearby domains. **(D–F)** depict similar plots as in (A), (B) and (C), respectively. The only difference is that here we compare the experimental and ML recreated Hi-C matrix for ΔMukBEF22MM. From figure (F), it is evident that there are long-range contacts across all MDs except the Ter, suggesting that the ML-derived matrix cannot accurately capture the long-range reduction of contacts for all MDs except the Ter.

these matrices. However, a closer examination of the difference heatmap (Figure 7F) reveals long-range contacts across all MDs, except for the Ter MD (highlighted by the magenta box). This observation suggests that the recreated matrix fails to appropriately capture the long-range reduction of interactions for all domains except the Ter.

The unsupervised ML model operates within the constraints of the information it has been exposed to during training, unable to generate entirely novel insights beyond its training data. Essentially, it excels at recognizing patterns within the provided datasets. Consequently, when the model is trained solely on the WT Hi-C matrix without exposure to mutant data, it inevitably falls short in accurately capturing the modified interactions specific to mutants compared to the WT type. For instance, in the recreation of the ΔMatP30MM Hi-C matrix, the model fails to adequately capture the nuanced interactions within the Ter and its flanking MDs. Similarly, for the ΔMukBEF22MM Hi-C matrix, the model fails to accurately represent the reduction in long-range interactions for all MDs, except the Ter. Interestingly, the WT training model manages to capture various other intrinsic information crucial for recreating mutant Hi-C matrices. To support this, we have trained the same model with a random matrix whose diagonal elements are 1 and all other elements are between (0−1) (see Method section). Attempting to reconstruct the ΔMatP30MM with this trained model resulted in an extremely poor PCC of 0.03 (Supplementary Figure S5). Together these results suggest that our unsupervised ML model (Autoencoder) provides a powerful way to reconstruct the Hi-C of the mutant which is semi-quantitatively accurate.

How close does the ML-derived model replicate the dynamics of different mutants?

In our earlier discussion on the intrinsic structural patterns within the Hi-C matrix, we observed that the WT training model effectively captures the mutant Hi-C matrices in a semi-quantitative manner. Now, our focus is on predicting the dynamics of chromosomal loci for various mutants using the training model on WT data. In this scenario, the model utilizes previously trained 'decision trees' to predict the dynamics. Supplementary Figure S6 shows the PCC(ρ) between the actual and predicted MSDs over time for both WT and mutant (ΔMatP30MM and ΔMukBEF22MM) chromosomes. The figure indicates that the correlations for both mutants are lower compared to the WT chromosome. Additionally, the correlation for ΔMukBEF22MM deviates more from WT compared to ΔMatP30MM, suggesting that the WT training model is less accurate in capturing loci dynamics for ΔMukBEF22MM. A closer examination of the Hi-C matrices for WT and mutant cases reveals distinct patterns. For ΔMatP30MM, the contact probability in the Ter and its flanking domains deviates from the WT matrix. In contrast, for ΔMukBEF22MM, the contact probability for all macrodomains deviates from the WT matrix, except for Ter MD. This suggests that when training the model with the WT matrix, it captures information more useful for predicting the dynamics of ΔMatP30MM compared to ΔMukBEF22MM. Consequently, when predicting the chromosome dynamics for ΔMatP30MM using WT training data, the deviation in correlation is less compared to ΔMukBEF22MM.

To understand the differences in the dynamics derived from a trained model with WT, we have calculated the key features for mutant bacteria using the same protocol as for wild-type bacteria. After training a random forest regression model with distance-based features and MSD values as labels for mutant bacteria, we have identified the important features for these two mutants. Supplementary Figures S7A and S7B show the MD-wise feature importance of the *top features* for ΔMatP30MM and ΔMukBEF22MM, respectively. These plots suggest that the MD-wise contribution of the *top features* is similar to that of wild-type bacteria. However, quite interestingly, the total number of *top features* for mutant bacteria differs from that of wild-type bacteria. Specifically, the number of *top features* is 383 for ΔMatP30MM, compared to 466 for wild-type bacteria, and 323 for ΔMukBEF22MM. To better understand the contribution of *top features*, we have computed the MD-wise contribution of the *top features* with respect to the total number of features (928) instead of the total number of *top features*. Supplementary Figure S7C represents the percentage-wise contribution of top features for each MD for wild-type and mutant bacteria. This plot indicates that for mutant bacteria, the percentage-wise contribution for each MD is lower compared to wild-type bacteria. These observations suggest that the *top features* governing the dynamics in mutant bacteria are different from those in wild-type bacteria. This difference might be a crucial factor for the deviation in the dynamics predicted from wild-type training data for mutant bacteria.

Discussions and summary

The organization and dynamics of the bacterial DNA are very complex and not yet fully explored. To address this, the utilization of the Hi-C integrated (21–24,44) and cross-linked (45,46) based polymer model offers a versatile means of exploring the organization and dynamics of *E. coli* DNA. In this study, we present a comprehensive approach, employing a set of machine learning (ML) algorithms to gain insights into the structural and dynamical aspects of bacterial chromosome. By leveraging a combination of Autoencoder-based structural analysis, and RF regression for predicting chromosomal dynamics, our work provides valuable insights into an intricate pattern of bacterial chromosomal organization and it emergent dynamics.

In the first part of the study, we mainly focused on extracting essential structural information, that is hidden underneath the Hi-C matrix, using an unsupervised deep neural network known as Autoencoder. The low-dimensional representation of the Hi-C data interestingly identifies chromosomal macrodomains (MDs) as key structural pattern in an automated way (Figures 2). Notably, the comparison between MDs derived from our ML model (Autoencoder) and those experimentally identified reveals a high correlation, suggesting meaningful connections between the ML-derived insights and real-world biological phenomena. However, Figure 2B suggests that there are significant differences exist between the ML-derived and the experimentally denoted MDs, particularly in the Right and Ter regions. We speculated that utilizing a higher-dimensional latent space could enhance the results. To test this hypothesis, we clustered the data in a four-dimensional latent space ($L_d = 4$). In Supplementary Figure S8(A), a comparison between the ML-derived and experimentally identified MDs for a latent dimension of $L_d = 4$ is presented, revealing notable improvements in MDs classification compared to $L_d = 3$. Furthermore, we quantified this enhancement by computing the F1-score for each MD.

Supplementary Figure S8B shows the comparison of F1-scores across different MDs for two latent dimensions (L_d = 3, 4). While there is a slight decrease in the F1-score for Left, NSL and Ori, significant improvements are observed for the other three MDs. The overall accuracy is 0.87 for $L_d = 4$, compared to 0.82 for $L_d = 3$. Although the higher dimension latent space provides the improvement in the results, the visualization of the latent space in 4d is not possible. Therefore, we kept all of the analysis in latent dimension L_d = 3. Additionally, there exist various other Autoencoder techniques like Denoising Autoencoder (47), Variational Autoencoder (48), etc. The usage of these advanced techniques could potentially improve the overall identification of the MDs. Moreover, when recreating the Hi-C matrix for various mutants using wild-type (WT) training data (Figures 7), our model demonstrates the ability to capture diverse intrinsic information crucial for reconstructing mutant Hi-C matrices. Significantly, the observed structural properties closely align with established experimental findings, underscoring the effectiveness of our approach in capturing biologically relevant phenomena.

In general, the partitioning of the eukaryotic chromosome into A and B compartments is achieved through principal component analysis (PCA) (15,26). We have also employed PCA to identify macrodomains for *E. coli*. Subsequently, we clustered the data for the first three principal components (PC-1, PC-2 and PC-3) using the K-means clustering algorithm. Supplementary Figure S9(A) presents a schematic representation of the macrodomains derived from machine learning (Autoencoder), PCA and experimental data. To compare how the PCA and ML-derived macrodomains match with experimentally identified macrodomains, we calculated the F1-Score for both methods (PCA, Autoencoder). Supplementary Figure S9(B) shows a comparison of the F1-Scores for macrodomains derived from these two techniques. This figure suggests that the Autoencoder outperforms PCA in identifying macrodomains, particularly for four specific regions: NSR, Left, NSl and Ori. However, for two other regions, PCA performs better than the Autoencoder. Nevertheless, the overall accuracy for identifying macrodomains using PCA is 67%, while the overall accuracy for the Autoencoder is 82%. Thus, the utilization of the ML-based non-linear technique Autoencoder provides a superior method for identifying macrodomains compared to the traditional linear technique PCA. There are also other advantages of using the Autoencoder over PCA, such as the ability to recreate the mutant matrix from wild-type training data. This helps in understanding the inherent information contained in the wild-type matrix, which is important for studying mutant bacteria. While PCA allows for the projection of mutant data along the principal components of the wild-type matrix, it does not enable the recreation of the mutant matrix.

After delving into the structural insights extracted from the Hi-C data, the second part of our study focused on harnessing the power of ML to predict the crucial subsets of chromosomal contact features that can optimally explain the previously reported heterogeneous subdiffusion of chromosomal loci. We employed a Hi-C embedded polymer model for the *E. coli* chromosome, representing short and long-range Hi-C contacts as effective springs with spring constants dependent on contact probabilities. Subsequently, we utilized RF regression, a powerful supervised machine learning algorithm, to predict the dynamics and MSD exponent of individual chromosomal loci. Our results demonstrated a high correlation between the predicted and actual MSD values for shorter time scales (Figures 4). These observations highlight the efficacy of our machine learning model in capturing the complex relationship between structural features and dynamic behavior. However, at a large time scale, the correlation between the actual and predicted values decreases. We hypothesized that at larger time scales, the system loses its initial structural information, leading to a reduction in correlation. Despite this decrease, it remained relatively modest.

We systematically evaluated the robustness of our RF regression model by varying hyperparameters (Supplementary Figures S1). The consistent performance across different hyperparameter values affirmed the reliability of our machine-learning approach. An essential aspect of our study involved extracting *top features* through feature importance analysis, providing valuable insights into the critical elements influencing chromosomal dynamics. However, these *top features* are dynamic rather than static, exhibiting variations over time (Figure 5A–D). The distribution of *top features* at a particular time across different macrodomains revealed non-uniform contributions (Figure 5E). Particularly, the Ori macrodomain exhibited a more substantial contribution compared to the right macrodomain. This non-uniformity was further elucidated by examining the distribution of MSD values for different macrodomains, with Ori displaying a broader distribution (Figure 5F). These findings indicate that the model requires more features to accurately capture dynamics when faced with a broader distribution of training data. Moreover, by incorporating the *top features* associated with Hi-C contacts into a polymer-based model, we can effectively reconstruct both the experimental Hi-C matrix and the dynamical behavior of chromosomal loci at a short time scale (Figures 6). These findings strongly imply the utility of our RF regression model for feature engineering, specifically in extracting the important Hi-C contacts that play a crucial role in influencing chromosomal dynamics. However, our model does have limitations; for instance, it may not fully capture interactions specific to mutants as it is trained solely on wild-type data.

Our work enhances the broader understanding of bacterial chromosome via computational modeling with ML techniques. The identification of macrodomains and the prediction of chromosomal dynamics offer a comprehensive view of the intricate interplay between structure and function in bacterial genomes. However, our approach can be extended beyond the realm of bacterial chromosomes. We are optimistic about the broader applicability of our methodologies in addressing more complex systems, including proteins and glass, to extract structural insights and predict dynamics. In the realm of glassy systems, there has recently been a plethora of studies predicting dynamics using a combination of structural properties and diverse machine-learning algorithms (49–56). While many of these studies leverage a multitude of structural features for dynamic predictions, we hope that our approach may offer an effective avenue for predicting dynamics and facilitating feature engineering.

Methods

The training of the Autoencoder

The Autoencoder in our study consists of nine fully connected sequential layers. We have used a single Hi-C contact probability matrix for training the Autoencoder. We utilize the

Leaky rectified linear unit (ReLU) activation function for each layer, except for the last layer. Given that our Hi-C contacts fall within the range of 0 to 1, the sigmoid activation function is applied to the final layer. To optimize the weights and biases of each node, we utilize the Adam optimizer (57) to minimize the loss function. We choose binary cross-entropy (BCE) (27,58) as a loss function which is defined as

$$-\sum_{i=1}^{N}\left(O_i \log\left(\hat{O}_i\right) + (1-O_i)\log\left(1-\hat{O}_i\right)\right) \quad (4)$$

where $\hat{O}$, and O are the model output, target output, and $N = 928$ respectively. The Autoencoder is trained with a batch size of 30 for input data and a learning rate of 0.001. Notably, in training the Autoencoder on the Random matrix, we have used the same architecture, modifying only the dimension of the latent space L_d. Our observations indicate that achieving a Pearson Correlation Coefficient (PCC) value of 0.79 between the actual random matrix and the Autoencoder-derived matrix necessitates setting L_d to 40 (Supplementary Figure S10). All aspects related to the Autoencoder, including training and implementation, are conducted using the Python implementation of Tensorflow (59) and Keras (60).

Training-testing split

In our ML model (RF), we allocate 75% of the data for training and 25% for testing. This partitioning ensures that the dimensions of the training and testing data are as follows: $\text{features}_{\text{training}}[m, n] = [\text{runs} \times 928, 928] = [150 \times 928, 928]$, $\text{labels}_{\text{training}}[m] = [\text{runs} \times 928] = [150 \times 928]$ and $\text{features}_{\text{testing}}[m, n] = [\text{runs} \times 928, 928] = [50 \times 928, 928]$, $\text{labels}_{\text{testing}}[m] = [\text{runs} \times 928] = [50 \times 928]$.

Simulation model details

We have applied our previously established bead-spring model (21,22) for integrating Hi-C data in *E. coli* chromosome, where each bead corresponds to 5×10^3 bp (5 kb). The harmonic interaction between adjacent beads is governed by a spring constant of $k_{spring} = 300 k_B T/\sigma^2$, where σ denotes the bead diameter. The inclusion of Hi-C contacts in the polymer chain introduces an effective spring with a spring constant dependent on contact probabilities. This process involves: (i) transforming the Hi-C probability matrix into a distance matrix using the formula:

$$D_{ij} = \sigma / P_{ij} \quad (5)$$

where i and j are the row and column index of the matrix respectively. (ii) By using D_{ij}, we have calculated the effective spring constant as:

$$k_{ij} = k_0 e^{-\frac{(D_{ij}-\sigma)^2}{w^2}} \quad (6)$$

Here, k_0 serves as the upper bound of the spring constant, and w^2 is a constant value. However, previous studies (61,62) on eukaryotes suggest that the relationship between D_{ij} and P_{ij} follows $D_{ij} = \sigma/P_{ij}^{1/3}$ or $D_{ij} = \sigma/P_{ij}^{1/4}$. We have also verified that these types of relationships yield similar dynamic behavior of the chromosomal loci with proper optimization of w^2 value. In our simulation, we have maintained the values of k_0 and w^2 consistent with our previous study (21,22), specifically $k_0 = 10 k_B T/\sigma^2$ and $w^2 = 0.3$. The potential related to Hi-C contacts, denoted as $E_{Hi-C}(r_{ij})$, is expressed as:

$$E_{Hi-C}(r_{ij}) = \frac{1}{2} k_{ij} (D_{ij} - r_{ij})^2 \quad (7)$$

In our simulation, contacts with a spring constant $k_{ij} < 10^{-7}$ are disregarded to avoid unnecessary low-value contacts. additionally, the nonbonded interactions between beads are modeled using the repulsive part of the Lenard-Jones potential, i.e., $E_{nb} = 4\epsilon(\frac{\sigma}{r})^{12}$. All particles are confined within a spherocylinder, mimicking the cell wall, with a length of $L = 45.754\sigma$ and diameter $d = 12.181\sigma$. The confinement potential is defined as:

$$E_{res}(r, R_0) = \frac{1}{2} k_{res} \left|\vec{r} - \vec{R}_0\right|^2 \Theta \left|\vec{r} - \vec{R}_0\right| \quad (8)$$

Here, R_0 represents the center of the spherocylinder, and k_{res} is the spring constant controlling confinement softness (set to $310 k_B T/\sigma^2$). The step function Θ activates if any particle surpasses the confinement boundaries. The total Hamiltonian of the system is given by:

$$H_{tot} = E_b + E_{Hi-C} + E_{nb} + E_{res} \quad (9)$$

Here, E_b, E_{Hi-C}, E_{nb} and E_{res} represent the potentials for bonded, Hi-C restraining, non-bonded, and confinement restraining interactions, respectively. All the simulations were conducted using an modified version of open-source software GROMACS 5.0.6 (63), while for the implementation of random forest regression, we utilized the Python library known as scikit-learn (64).

Calculation of Hi-C contacts

We have calculated the Hi-C matrix using our simulation trajectories. For each time series configuration, we have computed the pairwise distance D_{ij} between each bead and then converted the distance into a probability value using the formula $P_{ij} = \sigma/D_{ij}$, where σ is the diameter of each bead, and i and j are the bead indices. Finally, we have averaged these probability values over all the frames and trajectories.

Data availability

All data are present within the manuscript. The code and accompanying documentation for training the Autoencoder and Random Forest regression model can be accessed through GitHub at the following URL: https://github.com/palash892/Hi-C_ML_structure-dynamics (also archived in Zenodo at https://doi.org/10.5281/zenodo.13312410).

Supplementary data

Supplementary Data are available at NAR Online.

Acknowledgements

All the authors acknowledge Tata Institute of Fundamental Research Hyderabad, India for providing the support of computing resources. We acknowledge support of the Department of Atomic Energy, Government of India, under Project Identification No. RTI 4007.

Funding

Tata Institute of Fundamental Research Hyderabad, India; Department of Atomic Energy, Government of India [RTI 4007]. Funding for open access charge: Intramural research.

Conflict of interest statement

None declared.

References

1. Volkmer,B. and Heinemann,M. (2011) Condition-dependent cell volume and concentration of Escherichia coli to facilitate data conversion for systems biology modeling. *PloS One*, **6**, e23126.
2. Reshes,G., Vanounou,S., Fishov,I. and Feingold,M. (2008) Timing the start of division in E. coli: a single-cell study. *Phys. Biol.*, **5**, 046001.
3. Grainger,D.C., Hurd,D., Harrison,M., Holdstock,J. and Busby,S.J. (2005) Studies of the distribution of Escherichia coli cAMP-receptor protein and RNA polymerase along the E. coli chromosome. *Proc. Natl. Acad. Sci. U.S.A.*, **102**, 17693–17698.
4. Wiggins,P.A., Cheveralls,K.C., Martin,J.S., Lintner,R. and Kondev,J. (2010) Strong intranucleoid interactions organize the Escherichia coli chromosome into a nucleoid filament. *Proc. Natl. Acad. Sci. U.S.A.*, **107**, 4991–4995.
5. Badrinarayanan,A., Reyes-Lamothe,R., Uphoff,S., Leake,M.C. and Sherratt,D.J. (2012) In vivo architecture and action of bacterial structural maintenance of chromosome proteins. *Science*, **338**, 528–531.
6. Bakshi,S., Siryaporn,A., Goulian,M. and Weisshaar,J.C. (2012) Superresolution imaging of ribosomes and RNA polymerase in live Escherichia coli cells. *Mol. Microbiol.*, **85**, 21–38.
7. Niki,H., Yamaichi,Y. and Hiraga,S. (2000) Dynamic organization of chromosomal DNA in Escherichia coli. *Genes Dev.*, **14**, 212–223.
8. Valens,M., Penaud,S., Rossignol,M., Cornet,F. and Boccard,F. (2004) Macrodomain organization of the Escherichia coli chromosome. *EMBO J.*, **23**, 4330–4341.
9. Espéli,O. and Boccard,F. (2006) Organization of the Escherichia coli chromosome into macrodomains and its possible functional implications. *J. Struct. Biol.*, **156**, 304–310.
10. Espeli,O., Mercier,R. and Boccard,F. (2008) DNA dynamics vary according to macrodomain topography in the E. coli chromosome. *Mol. Microbiol.*, **68**, 1418–1427.
11. Mercier,R., Petit,M.-A., Schbath,S., Robin,S., El Karoui,M., Boccard,F. and Espéli,O. (2008) The MatP/matS site-specific system organizes the terminus region of the E. coli chromosome into a macrodomain. *Cell*, **135**, 475–485.
12. Messerschmidt,S.J. and Waldminghaus,T. (2015) Dynamic organization: chromosome domains in Escherichia coli. *J. Mol. Microbiol. Biotechnol.*, **24**, 301–315.
13. Dekker,J., Rippe,K., Dekker,M. and Kleckner,N. (2002) Capturing chromosome conformation. *science*, **295**, 1306–1311.
14. Dostie,J., Richmond,T.A., Arnaout,R.A., Selzer,R.R., Lee,W.L., Honan,T.A., Rubio,E.D., Krumm,A., Lamb,J., Nusbaum,C., *et al.* (2006) Chromosome Conformation Capture Carbon Copy (5C): a massively parallel solution for mapping interactions between genomic elements. *Genome res.*, **16**, 1299–1309.
15. Lieberman-Aiden,E., Van Berkum,N.L., Williams,L., Imakaev,M., Ragoczy,T., Telling,A., Amit,I., Lajoie,B.R., Sabo,P.J., Dorschner,M.O., *et al.* (2009) Comprehensive mapping of long-range interactions reveals folding principles of the human genome. *Science*, **326**, 289–293.
16. Lioy,V.S., Cournac,A., Marbouty,M., Duigou,S., Mozziconacci,J., Espéli,O., Boccard,F. and Koszul,R. (2018) Multiscale structuring of the E. coli chromosome by nucleoid-associated and condensin proteins. *Cell*, **172**, 771–783.
17. Weber,S.C., Spakowitz,A.J. and Theriot,J.A. (2010) Bacterial chromosomal loci move subdiffusively through a viscoelastic cytoplasm. *Phys. Rev. Lett.*, **104**, 238102.
18. Weber,S.C., Theriot,J.A. and Spakowitz,A.J. (2010) Subdiffusive motion of a polymer composed of subdiffusive monomers. *Phys. Rev. E*, **82**, 011913.
19. Javer,A., Long,Z., Nugent,E., Grisi,M., Siriwatwetchakul,K., Dorfman,K.D., Cicuta,P. and Cosentino Lagomarsino,M. (2013) Short-time movement of E. coli chromosomal loci depends on coordinate and subcellular localization. *Nat. Commun.*, **4**, 3003.
20. Weber,S.C., Spakowitz,A.J. and Theriot,J.A. (2012) Nonthermal ATP-dependent fluctuations contribute to the in vivo motion of chromosomal loci. *Proc. Natl. Acad. Sci. U.S.A.*, **109**, 7338–7343.
21. Wasim,A., Gupta,A. and Mondal,J. (2021) A Hi–C data-integrated model elucidates E. coli chromosome's multiscale organization at various replication stages. *Nucleic Acids Res.*, **49**, 3077–3091.
22. Bera,P., Wasim,A. and Mondal,J. (2022) Hi-C embedded polymer model of Escherichia coli reveals the origin of heterogeneous subdiffusion in chromosomal loci. *Phys. Rev. E*, **105**, 064402.
23. Wasim,A., Gupta,A., Bera,P. and Mondal,J. (2023) Interpretation of organizational role of proteins on E. coli nucleoid via Hi-C integrated model. *Biophys. J.*, **122**, 63–81.
24. Wasim,A., Bera,P. and Mondal,J. (2024) Development of a data-driven integrative model of a bacterial chromosome. *J. Chem. Theor. Comput.*, **20**, 1673–1688.
25. Bintu,B., Mateo,L.J., Su,J.-H., Sinnott-Armstrong,N.A., Parker,M., Kinrot,S., Yamaya,K., Boettiger,A.N. and Zhuang,X. (2018) Super-resolution chromatin tracing reveals domains and cooperative interactions in single cells. *Science*, **362**, eaau1783.
26. Rao,S.S., Huntley,M.H., Durand,N.C., Stamenova,E.K., Bochkov,I.D., Robinson,J.T., Sanborn,A.L., Machol,I., Omer,A.D., Lander,E.S. and et,al. (2014) A 3D map of the human genome at kilobase resolution reveals principles of chromatin looping. *Cell*, **159**, 1665–1680.
27. Xiong,K. and Ma,J. (2019) Revealing Hi-C subcompartments by imputing inter-chromosomal chromatin interactions. *Nat. commun.*, **10**, 5069.
28. Ashoor,H., Chen,X., Rosikiewicz,W., Wang,J., Cheng,A., Wang,P., Ruan,Y. and Li,S. (2020) Graph embedding and unsupervised learning predict genomic sub-compartments from HiC chromatin interaction data. *Nat. Commun.*, **11**, 1173.
29. Zhang,Y., An,L., Xu,J., Zhang,B., Zheng,W.J., Hu,M., Tang,J. and Yue,F. (2018) Enhancing Hi-C data resolution with deep convolutional neural network HiCPlus. *Nat. Commun.*, **9**, 750.
30. Hong,H., Jiang,S., Li,H., Du,G., Sun,Y., Tao,H., Quan,C., Zhao,C., Li,R., Li,W., *et al.* (2020) DeepHiC: A generative adversarial network for enhancing Hi-C data resolution. *PLoS Comput. Biol.*, **16**, e1007287.
31. Fudenberg,G., Kelley,D.R. and Pollard,K.S. (2020) Predicting 3D genome folding from DNA sequence with Akita. *Nat. Methods*, **17**, 1111–1117.
32. Liou,C.-Y., Cheng,W.-C., Liou,J.-W. and Liou,D.-R. (2014) Autoencoder for words. *Neurocomputing*, **139**, 84–96.
33. Zhai,J., Zhang,S., Chen,J. and He,Q. (2018) Autoencoder and its various variants. In: *2018 IEEE international conference on systems, man, and cybernetics (SMC)*. IEEE, pp. 415–419.
34. Likas,A., Vlassis,N. and Verbeek,J.J. (2003) The global k-means clustering algorithm. *Pattern Recogn.*, **36**, 451–461.
35. Kodinariya,T.M. and Makwana,P.R., *et al.* (2013) Review on determining number of cluster in K-means clustering. *Int. J.*, **1**, 90–95.
36. Breiman,L. (2001) Random forests. *Mach. Learn.*, **45**, 5–32.
37. Breiman,L. (2017) In: *Classification and Regression Trees*. Routledge.
38. Widmer-Cooper,A., Harrowell,P. and Fynewever,H. (2004) How reproducible are dynamic heterogeneities in a supercooled liquid?. *Phys. Rev. Lett.*, **93**, 135701.
39. Widmer-Cooper,A. and Harrowell,P. (2007) On the study of collective dynamics in supercooled liquids through the statistics of the isoconfigurational ensemble. *J. Chem. Phys.*, **126**, 154503.

40. Luijsterburg,M.S., Noom,M.C., Wuite,G.J. and Dame,R.T. (2006) The architectural role of nucleoid-associated proteins in the organization of bacterial chromatin: a molecular perspective. *J. Struct. Biol.*, **156**, 262–272.
41. Azam,T.A. and Ishihama,A. (1999) Twelve species of the nucleoid-associated protein from Escherichia coli: sequence recognition specificity and DNA binding affinity. *J. Biol. Chem.*, **274**, 33105–33113.
42. Dupaigne,P., Tonthat,N.K., Espéli,O., Whitfill,T., Boccard,F. and Schumacher,M.A. (2012) Molecular basis for a protein-mediated DNA-bridging mechanism that functions in condensation of the E. coli chromosome. *Mol. Cell*, **48**, 560–571.
43. Nolivos,S. and Sherratt,D. (2014) The bacterial chromosome: architecture and action of bacterial SMC and SMC-like complexes. *FEMS Microbiol. Rev.*, **38**, 380–392.
44. Messelink,J.J., van Teeseling,M.C., Janssen,J., Thanbichler,M. and Broedersz,C.P. (2021) Learning the distribution of single-cell chromosome conformations in bacteria reveals emergent order across genomic scales. *Nat. Commun.*, **12**, 1963.
45. Subramanian,S. and Murray,S.M. (2023) Subdiffusive movement of chromosomal loci in bacteria explained by DNA bridging. *Phys. Rev. Res.*, **5**, 023034.
46. Agarwal,T., Manjunath,G., Habib,F. and Chatterji,A. (2019) Bacterial chromosome organization. II. Few special cross-links, cell confinement, and molecular crowders play the pivotal roles. *J. Chem. Phys.*, **150**, 144909.
47. Vincent,P., Larochelle,H., Bengio,Y. and Manzagol,P.-A. (2008)] Extracting and composing robust features with denoising autoencoders. In: *Proceedings of the 25th International Conference on Machine Learning*. pp. 1096–1103.
48. Kingma,D.P. and Welling,M. (2013) Auto-encoding variational Bayes. arXiv doi: https://arxiv.org/abs/1312.6114, 20 December 2013, preprint: not peer reviewed.
49. Bapst,V., Keck,T., Grabska-Barwińska,A., Donner,C., Cubuk,E.D., Schoenholz,S.S., Obika,A., Nelson,A.W., Back,T., Hassabis,D., *et al.* (2020) Unveiling the predictive power of static structure in glassy systems. *Nat. Phys.*, **16**, 448–454.
50. Boattini,E., Marín-Aguilar,S., Mitra,S., Foffi,G., Smallenburg,F. and Filion,L. (2020) Autonomously revealing hidden local structures in supercooled liquids. *Nat. Commun.*, **11**, 5479.
51. Boattini,E., Smallenburg,F. and Filion,L. (2021) Averaging local structure to predict the dynamic propensity in supercooled liquids. *Phys. Rev. Lett.*, **127**, 088007.
52. Alkemade,R.M., Smallenburg,F. and Filion,L. (2023) Improving the prediction of glassy dynamics by pinpointing the local cage. *J. Chem. Phys.*, **158**, 134512.
53. Alkemade,R.M., Boattini,E., Filion,L. and Smallenburg,F. (2022) Comparing machine learning techniques for predicting glassy dynamics. *J. Chem. Phys.*, **156**, 204503.
54. Shiba,H., Hanai,M., Suzumura,T. and Shimokawabe,T. (2023) BOTAN: BOnd TArgeting Network for prediction of slow glassy dynamics by machine learning relative motion. *J. Chem. Phys.*, **158**, 084503.
55. Schoenholz,S.S., Cubuk,E.D., Sussman,D.M., Kaxiras,E. and Liu,A.J. (2016) A structural approach to relaxation in glassy liquids. *Nat. Phys.*, **12**, 469–471.
56. Jung,G., Biroli,G. and Berthier,L. (2023) Predicting dynamic heterogeneity in glass-forming liquids by physics-inspired machine learning. *Phys. Rev. Lett.*, **130**, 238202.
57. Kingma,D.P. and Ba,J. (2014) Adam: a method for stochastic optimization. arXiv doi: https://arxiv.org/abs/1412.6980, 22 December 2014, preprint: not peer reviewed.
58. Creswell,A., Arulkumaran,K. and Bharath,A.A. (2017) On denoising autoencoders trained to minimise binary cross-entropy. arXiv doi: https://arxiv.org/abs/1708.08487, 09 October 2017, preprint: not peer reviewed.
59. Abadi,M., Agarwal,A., Barham,P., Brevdo,E., Chen,Z., Citro,C., Corrado,G.S., Davis,A., Dean,J., Devin,M., *et al.* (2016) Tensorflow: large-scale machine learning on heterogeneous distributed systems. arXiv doi: https://arxiv.org/abs/1603.04467, 16 March 2016, preprint: not peer reviewed.
60. Bisong,E. and Bisong,E. (2019) Tensorflow 2.0 and keras. In: *Building Machine Learning and Deep Learning Models on Google Cloud Platform: A Comprehensive Guide for Beginners*. pp. 347–399.
61. Kumari,K., Duenweg,B., Padinhateeri,R. and Prakash,J.R. (2020) Computing 3D chromatin configurations from contact probability maps by inverse Brownian dynamics. *Biophys. J.*, **118**, 2193–2208.
62. Shi,G. and Thirumalai,D. (2021) From Hi-C contact map to three-dimensional organization of interphase human chromosomes. *Phys. Rev. X*, **11**, 011051.
63. Abraham,M.J., Murtola,T., Schulz,R., Páll,S., Smith,J.C., Hess,B. and Lindahl,E. (2015) GROMACS: High performance molecular simulations through multi-level parallelism from laptops to supercomputers. *SoftwareX*, **1**, 19–25.
64. Pedregosa,F., Varoquaux,G., Gramfort,A., Michel,V., Thirion,B., Grisel,O., Blondel,M., Prettenhofer,P., Weiss,R., Dubourg,V., *et al.* (2011) Scikit-learn: machine learning in Python. *J. Mach. Learn. Res.*, **12**, 2825–2830.

Received: March 8, 2024. **Editorial Decision:** August 8, 2024. **Accepted:** August 19, 2024
© The Author(s) 2024. Published by Oxford University Press on behalf of Nucleic Acids Research.
This is an Open Access article distributed under the terms of the Creative Commons Attribution-NonCommercial License (https://creativecommons.org/licenses/by-nc/4.0/), which permits non-commercial re-use, distribution, and reproduction in any medium, provided the original work is properly cited. For commercial re-use, please contact reprints@oup.com for reprints and translation rights for reprints. All other permissions can be obtained through our RightsLink service via the Permissions link on the article page on our site—for further information please contact journals.permissions@oup.com.